Millimeter wave array-HIS antenna for imaging applications

A. Flórez Berdasco[1] · **M. E. de Cos Gómez[1]** · **H. Fernández Álvarez[1]** · **F. Las-Heras[1]**

Abstract

The combination of a patch array antenna with a High Impedance Surface (HIS) metasurface at mmWave frequencies has been studied. The antenna is intended for a collision avoidance imaging application, which will help blind or visually impaired people in their daily lives. A compact and cost-effective uniplanar design, operating in the mmWave unlicensed frequency band (24.05–24.25 GHz), has been reached. Multiple arrangements and dispositions of the HIS unit-cells with the array have been explored in order to improve the radiation parameters of the basic design. Both, the basic array and the array-HIS combination, have been manufactured using laser micromachining. Prototypes have been measured in an anechoic chamber and measurement results have been confronted with the simulation ones in terms of bandwidth and radiation properties. A comparison with the state-of-the-art antennas at 24 GHz has been performed to endorse the achievements of this work.

Keywords Antennas · mmWaves · HIS · Metasurface · Antenna with metasurface · Collision avoidance radar · Imaging

1 Introduction

Radar technology is used to detect objects, their distance and angular position and/or their speed [1]. Interest in millimeter waves has grown [2, 3] due to the increasing demand for bandwidth and channel capacity that has led to the incorporation of millimeter waves into the useful 5 G spectrum and the existence of an unlicensed frequency band at 24 GHz. In addition, this technology has been widely used in the automotive industry, for example with the development of advanced driver assistance systems (ADAS) [4], which have contributed to the evolution of millimeter wave radar technology, making it affordable [5].

One of the advantages of mmWave radars is that they provide higher resolution (the shorter the wavelength, the higher the resolution) than radars operating at lower frequencies, so that they can detect smaller objects. Moreover, as the frequency increases, they become more compact, which makes it an attractive technology for many applications [5]. However, mmWave propagation suffers high free space losses,

which are increased by vegetation, atmospheric gases and also the rain [6]. Furthermore, the attenuation suffered by mmWaves when penetrating on materials is higher than for microwaves [7]. Nevertheless, for short-range applications related to human safety, they are a good option, due to their non-ionizing nature. Additionally, they can pass through textiles, and they are robust against fog, smoke, or dust. Thus, mmWave radar technology is widely used in medicine [8], non-destructive evaluation [9] or defense and security [10]. Therefore, mmWave radars could be suitable to help blind or visual impaired people to avoid collisions in their daily lives.

As mentioned before, mmWave radars are mature especially in automotive industry. The 24 GHz frequency band is commonly used for short-range applications, like vulnerable side recognition, whereas for long-range applications such as cruise control, higher frequencies are used [11].

The antenna is a key element of the radar since it greatly impacts on the system performance. The main objective of this work is to design a wearable antenna at 24 GHz, to be used with a radar module in an assistive system to help blind and visually impaired people. The goal of this application is to detect obstacles in a few meters to avoid collisions. Furthermore, to improve the radiation parameters and/or the bandwidth of the antenna, it is intended to combine it with a metasurface in order to analyze the overall behavior of the structure.

✉ A. Flórez Berdasco
   florezalicia@uniovi.es

   M. E. de Cos Gómez
   medecos@uniovi.es

1 TSC Electrical Engineering Department, University of Oviedo, 33203 Gijón, Spain

Traditional radars used in aerospace need high directivity, which requires narrow beamwidth antennas, allowing longer range and better angular resolution [1], whereas if short-range detection is required, an antenna with an omnidirectional radiation pattern is preferred, for illuminating the whole scene in front of the radar from each possible position. Thus, a trade-off solution between coverage area and range must be adopted. Likewise, the selected frequency band is a compromise among resolution, range, and suitability of manufacturing.

In the previous literature, metasurfaces (a subset of metamaterials, which are 2D-periodic) have frequently been used to improve certain aspects of the antenna's performance [12–15]. In the case of microstrip patches, most authors use an Artificial Magnetic Conductor (AMC) arranged below the radiating element, in order to isolate it from the body further than the original ground plane, aiming at reducing the Specific Absorption Rate (SAR) and/or improve the radiation properties of the antenna. Others authors employed an Electromagnetic Band Gap (EBG) around the primitive antenna to reduce the surface waves. The first option involves the metasurface design attending to the phase of the reflection coefficient and its arrangement below the antenna considerably increases the thickness of the resulting device with respect to the initial [16–18]. The latter option entails the metasurface design in terms of its dispersion diagram, and it is mostly used to improve the radiation efficiency and/or to reduce the coupling between the array elements [19–21], in order to be able to place them closer than it is theoretically required for proper operation [22–24]. Nevertheless, in no case has it been possible to improve all the radiation parameters with respect to the original antenna and even less at the same time as the operating bandwidth.

When a finite number of unit-cells is arranged around the primitive antenna and working at microwaves or mmWaves frequencies, where the unit-cells are not so small compared with the wavelength, it seems more rigorous attend to the resonance frequency of the metasurface instead of named it EBG or AMC [in this work, rather than classifying the metasurface as one of the already existing ones, this structure will be characterize by its resonance frequency and superficial impedance value prior to the combination with the primitive antenna. In fact, the type of metasurface into which it could be rigorously classified is as a High Impedance Surface (HIS)]. Moreover, if an EBG is designed at 24.125 GHz, the size of the resulting cell would be greater than the one presented later, so that it cannot be arranged between the elements of the submitted array. It would be necessary to increase the separation between elements, obtaining a bigger antenna.

At the beginning, the infinite metasurface is analyzed to know its resonance frequency, since in some way it is necessary to start the design, and this is a rigorous and straight forward one. Even taking into account that when using only few unit-cells, the resonance frequency will slightly shift compared with the infinite structure. Besides, in this work both, the primitive antenna and the metasurface, are arranged in the same layer, so they will influence each other. Indeed, each unit-cell can be seen as a metallic-dielectric resonator [25].

This work focuses on the analysis of the impedance that the metasurface presents and how the current distribution of the unit-cells influence the the antenna one, and therefore, the radiation pattern. Thus, we aim at designing a High Impedance Surface (HIS), that being arranged around the array elements will improve all the radiation parameters and the bandwidth (in literature some parameters are improved while others not and/or with thickness increase) without increasing the size.

The paper is organized as follows: first, the design of the basic array is presented. Then, the metasurface design is shown. Next, the different combinations of the antenna with the metasurface are presented, including the analysis of the position of the unit-cells on each design. The different designs are then compared in terms of bandwidth and radiation properties. Subsequently, measured results of the fabricated prototypes are evaluated with those of the simulation. Finally, a comparison with the state-of-the-art antennas at 24 GHz and some conclusions are exposed.

2 Antenna design

The antenna must be light, compact, and comfortable due to the wearable application for which it is intended. Besides, it must be power efficient, a key for wearable in order to save battery, as well as cost efficient. Moreover, an antenna with low backward radiation is preferred to reduce the radiation to the person wearing it. As mentioned before, in order to illuminate the whole scene in front of the user at a time, an antenna with an omnidirectional radiation pattern is needed to detect all the obstacles. RO3003 (ε_r=3, tan$_\delta$=0.0013) has been chosen as the substrate for the antenna since its intermediate relative dielectric permittivity value allows getting a suitable size for the prototype. Unlike the frequency bands commonly used for wireless communications (below 6 GHz), at mmWaves fabrication is challenging itself, since the physical dimensions are reduced as the frequency rises. The difficulties increase if dielectrics with high relative dielectric permittivity are used, which further reduce the dimensions. In addition, this material turns out economical and suitable for manufacturing. In order to satisfy the previous requirements, a two-patch array has been design, which offers a quasi-omnidirectional radiation pattern but with higher directivity and gain than a simple patch, so

Table 1 Theoretical dimensions of the microstrip patch antenna

Wpatch [mm]	Lpatch [mm]	Wground [mm]	Lground [mm]
4.39	2.77	8.89	7.27

that it enables higher range. Table 1 shows the theoretical patch antenna dimensions for a frequency in the middle of the intended band (24.125 GHz) [26].

Microstrip technology has been chosen since its inherent ground plane reduces the backward radiation. 50Ω impedance has been selected for the feeding line. A corporate-fed power divider is included with the objective of feeding both patches. This type of structure is preferred over series-fed because it offers wider bandwidth, and it allows more freedom in spacing elements [27]. The well-known T-divider [28], has been taken as the starting point. This three-port network cannot be reciprocal, lossless and adapted on its three ports simultaneously to be realizable. In order to achieve a lossless power divider, a trade-off solution must be reach among the power divider dimension, the input matching, the insertion losses and the ports coupling. Due to the wearable nature of the application for which this antenna is intended, that requires compacting the design, straight bends have been replaced by optimal chamfered bends and the quarter-wave impedance transformers by tapering, which will reduce reflections produced at discontinuities, and therefore, insertion losses. It is necessary to highlight, that the patches do not present an input impedance of 50Ω, so that parametric sweeps with a commercial software have been carried out to optimize the complete structure. Figure 1a shows the geometry of the antenna with its dimensions. The resonance frequency is mainly controlled by Lp but also by some parts of the power divider as L50, L100, T2 and T3.

Table 2 indicates the final dimensions of the basic array, which have been obtained by a 3D FEM based electromagnetic simulation software. In order to avoid grating lobes, the separation between the patches of the basic array is $\sim 0.5 \lambda_0$.

2.1 Impedance matching

The simulation result for the reflection coefficient is shown in Fig. 1b. The basic array shows proper impedance matching from 23.2 to 24.9 GHz (7%), and thus it perfectly covers the intended incense free frequency band.

2.2 Radiation properties

Table 3 gathers the radiation properties of the basic array obtained in simulation at the resonance frequency and at the ends of the band. It is remarkable that the antenna shows a very high radiation efficiency all over the operating bandwidth. Moreover, the best front-to-back ratio (FTBR) is obtained at the resonance frequency.

The radiation pattern cuts of the basic array obtained in simulation are presented on Fig. 2. The H-plane exhibits high cross-polariazation (XP) level, except in the maximum radiation direction, where the XP is at least 10 dB below the copolarization (CP) trace. However, this high XP level is not critical for the intended application of this work. The E-plane exhibits a quasi-omnidirectional radiation pattern with a very good CP-XP relation.

3 Metasurface design

In order to reduce the coupling between the patches and improve the radiation parameters and/or the bandwidth of the basic array while keeping the radiation efficiency, a metasurface has been designed to be combined with the basic array. A HIS metasurface, made of a set of unit-cells consisting of a metallic geometry over a grounded dielectric, is designed. HIS are characterized by the high value of its surface impedance at a certain frequency when a wave impinges on them. This type of metasurface can be used to suppress surface waves and/or reflect incident waves in phase [13, 29].

In this work, a simple unit-cell geometry has been chosen, due to the manufacturing challenge of the frequency band in which it works. Figure 3c shows a squared metallization geometry for the unit-cell. Wp names the side dimension of the squared metallization, g refers to the gap distance between the metallization and the edge of the unit-cell (consequently the distance between consecutive metallization is 2 g) and P stands of the total dimensions of the unit-cell.

The unit-cell is designed with suitable dimensions to be arranged between the array patches. Likewise, a set of a small number of unit-cells will be placed around the patches. The resonance frequency of the finite metasurface is

Table 2 Basic Array dimensions [mm]

W50	L50	T	W100	L100	T2	L50	A	L50_feed
2.06	8	1.4	0.55	0.8	1.4	0.5	0.2	2.7
T3	Lm	Wm	Lp	Wp	h	L	W	–
1.5	1.8	0.62	4	4.7	0.8	25.9	25.4	–

Fig. 1 a Geometry of the basic array. **b** Reflection coefficient of the basic array antenna

a)

b)

Table 3 Radiation properties of the basic array

Freq [GHz]	D [dB]	G [dB]	η [%]	FTBR [dB]
23.2	7	6.5	90	14.3
24.1	7.4	7.3	98	18.7
24.9	8.2	7.7	99	13.6

expected to be shifted with respect to the one of the infinite simulated metasurface. Because of this, a wide HIS bandwidth behavior is sought, so that it includes the basic array one, even if the HIS resonance frequency slightly shifts for not being an ideal infinite metasurface. In view of these, a trade-off solution between the total size of the unit-cell and the bandwidth of HIS behavior must be reached.

The optimization of the unit-cell for the quoted requirements, has been conducted through simulation with periodic boundary conditions and a Floquet port excitation. This optimization has been carried out based on the phase of the reflection coefficient, since this metasurface exhibits in phase reflection in the operating bandwidth. Generally, it is considered that the operating bandwidth comprises the frequencies for which the phase of the reflection coefficient is between − 90∘ and 90° [30]. The final dimensions of the unit-cell are indicated in Table 4. Figure 3a shows the reflection coefficient phase of the HIS metasurface. The HIS exhibits a bandwidth of 11.1 GHz, from 22.9 to 34 GHz (39.4%) and it resonates at the frequency of 28.2 GHz. The surface impedance of the HIS, is presented in Fig. 3b. At the resonance frequency, the highest value of the surface impedance is obtained, as it could be expected.

Fig. 2 Radiation pattern cuts for the basic array at 24.1 GHz obtained in simulation. Blue traces stand of copolarization (CP) and the red ones for cross-polarization (XP)
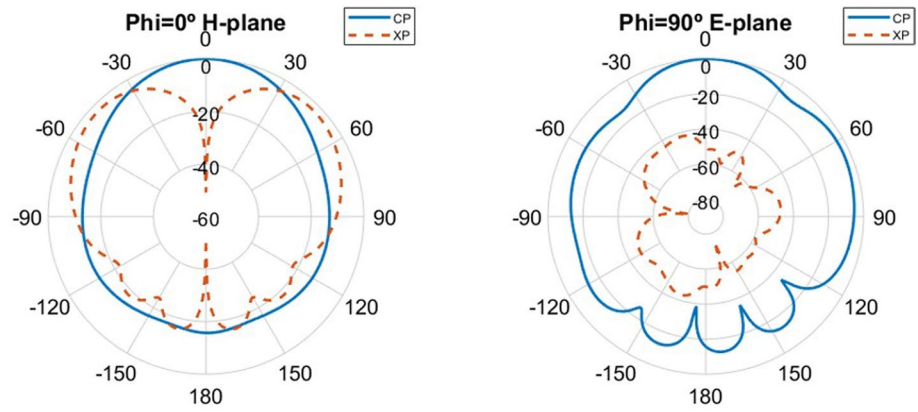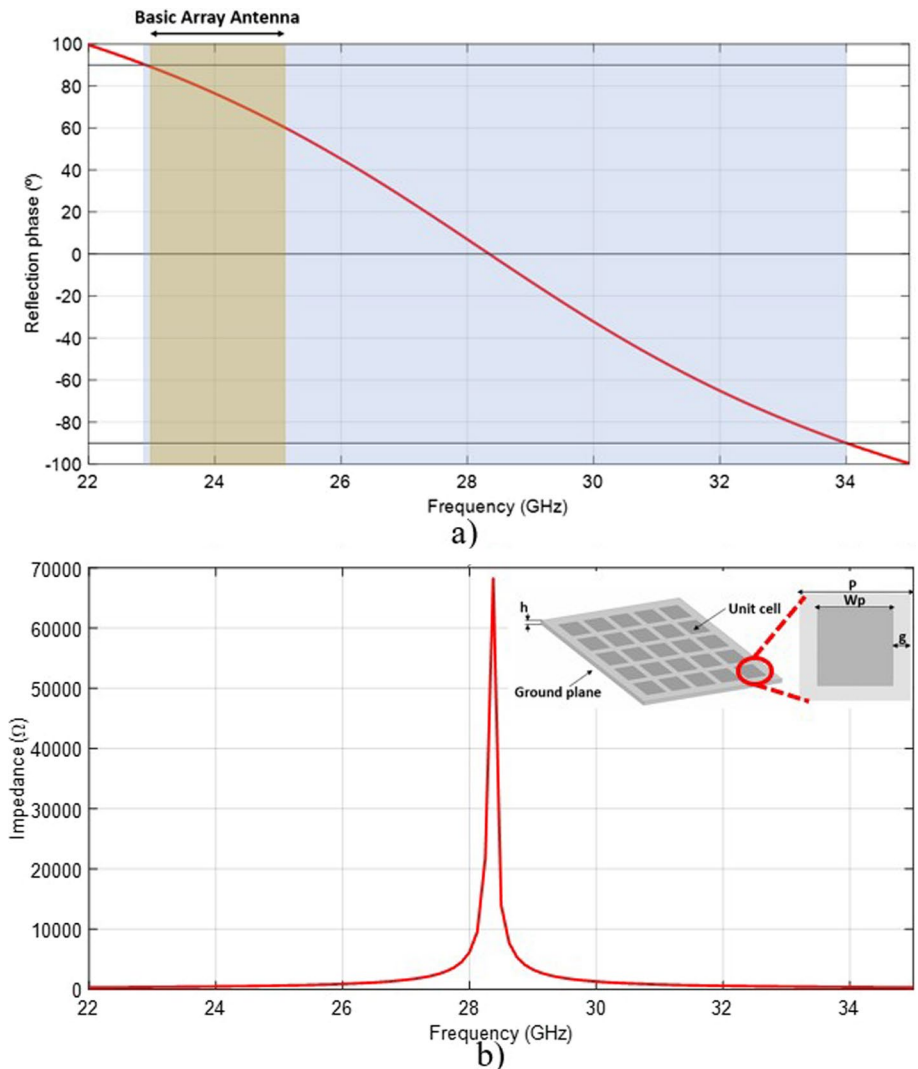
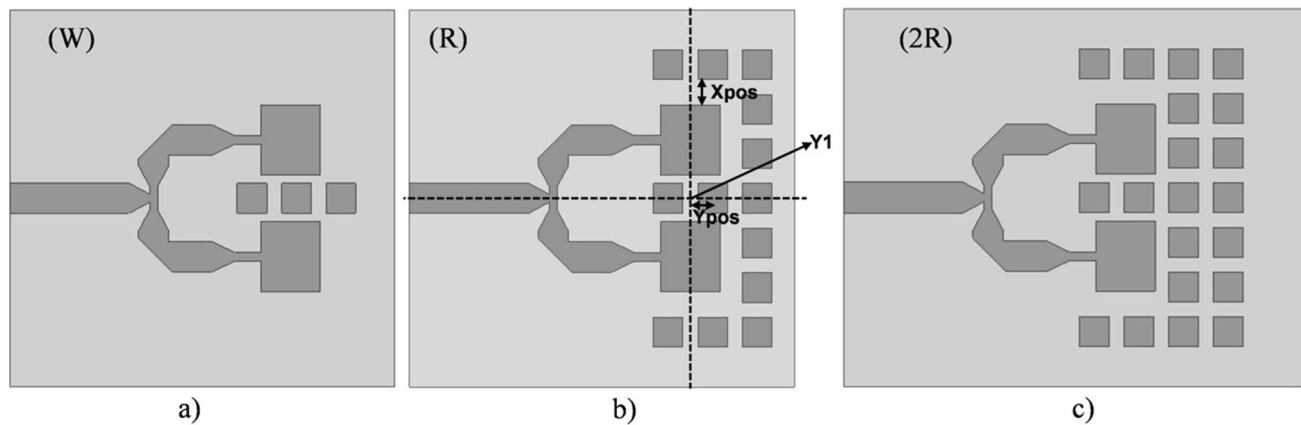

Table 4 Dimensions of the unit-cell

Wp [mm]	g [mm]	P [mm]	h [mm]
2	0.5	3	0.8

4 Array-HIS designs

Once both structures (patch array and HIS) operating in the desired frequency band are obtained, they are combined.

Fig. 3 **a** Reflection coefficient phase of the simulated HIS of the impinges plane wave. **b** Surface impedance of the HIS. **c** Structure of the HIS and unit-cell geometry

Fig. 4 Different arrangements of the HIS unit-cells around the basic array. **a** Wall (W), **b** Row (R), **c** 2Row (2R)

Three different arrangements of the HIS unit-cells placed in the same layer than the array patches have been analysed (see Fig. 4). In order to reduce the mutual coupling between the patches caused by being placed close to each other, a set of three unit-cells has been situated between them, as a kind of wall, in design (W) (see Fig. 4a). Design (R), which is shown in Fig. 4b, includes unit-cells around the patches so that the potential surface waves produced at the interface between two media, are diminished. Finally, a row of unit-cells is added in front of the patches (see Fig. 4c), in design (2R), to study its impact on the array performance.

4.1 Unit-cell position analysis for the wall design (W)

Firstly, the position of the unit-cells for the wall design (W), has been analyzed. An Y1 reference point has been defined as the intersection of a line crossing the feeding line and the HIS unit-cells in the y-axis direction and one dividing the patches in half in the x-axis direction (see Fig. 4a). Ypos is the parameter that indicates the position of the unit-cells. If Ypos=0 mm, the center of the unit-cell situated in the middle of the wall matches the reference point Y1. It is remarkable that the reference unit-cell will be the same for all the designs.

Table 5 presents the simulation results for the resonance frequency of 24.1 GHz. It can be observed that as the wall moves forward from Ypos=– 1 mm both, the radiation properties and the FTBR improve until they reach their optimum value at Ypos=1 mm, after which they worsen again. It is necessary to highlight that the position of the wall does not influence the radiation efficiency of the antenna.

Figure 5 shows the surface currents for the optimum (1 mm) and worst (– 1 mm) positions of the wall. Figure 5a and b present the surface current for a phase of 90∘. The surface current in the power divider is similar for both designs,

Table 5 Analysis of the wall position

Ypos [mm]	BW [%]	D [dB]	G [dBi]	η [%]	FTBR [dB]
-1	6.5	7.9	7.9	100	18.9
–0.5	6.7	7.9	7.9	100	18.8
0	6.8	8	8	100	19
0.5	6.7	8.1	8.1	100	24.5
1	6.8	8.2	8.2	100	25.4
1.5	6.5	8.1	8.1	100	24.4
2	6.6	8	8	100	24.4

whereas the values in the patches and unit-cells are higher for the position of the wall of Ypos=1 mm. The same behavior is observed for a phase of 230° (see Fig. 5c and d), showing higher levels for Ypos=1 mm in the patches as well as in the metasurface, which improves the radiation properties.

4.2 Unit-cell position analysis for the one row design (R)

The same analysis has been carried out for the design in which the array is surrounded by one row of unit-cells (see Table 6). As the cells move away from the patches, the FTBR improves until reaching an optimal value when Ypos=1 mm, while directivity and gain are slightly reduced. Continue increasing Ypos, does not improve but the contrary. The bandwidth and the radiation efficiency remain stable for all the values studied.

4.3 Unit-cell position analysis for the two rows design (2R)

The analysis has been repeated in order to study the influence of the unit-cells position in the design including two

Fig. 5 Surface current. **a**
Phase=90°, Ypos=– 1 mm.
b Phase=90°, Ypos=1 mm. **c**
Phase=230°, Ypos=– 1 mm. **d**
Phase=230°, Ypos=1 mm
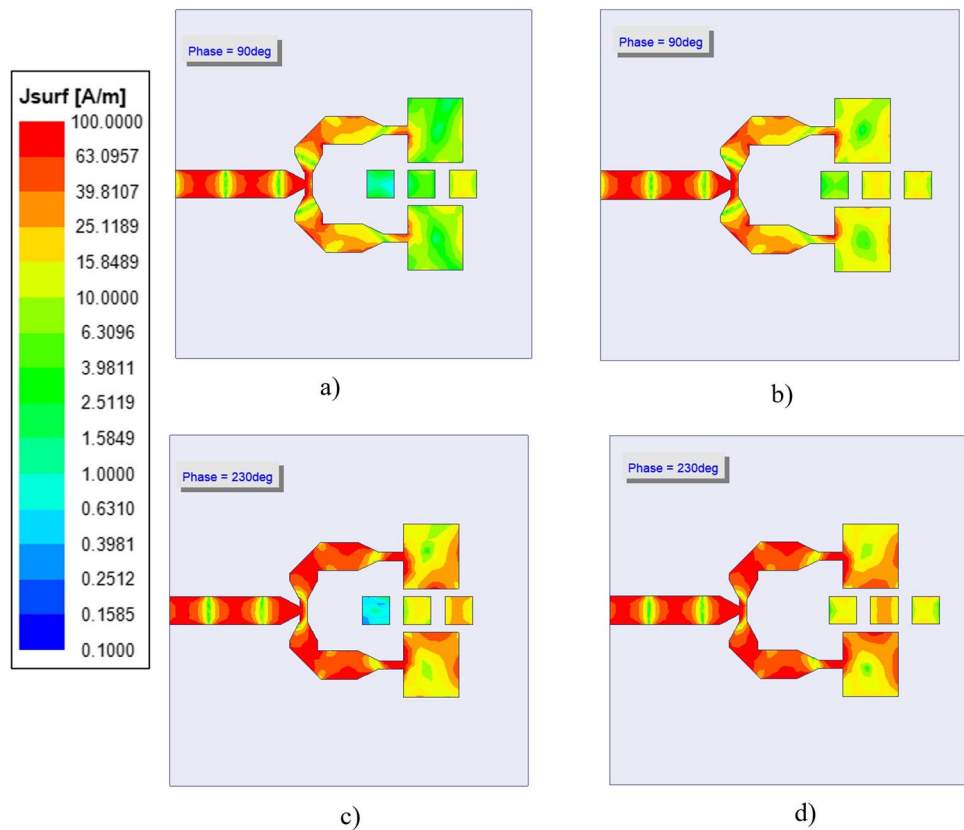
Table 6 Analysis of the position of the unit-cells for the design surrounded by a row

Ypos [mm]	BW [%]	D [dB]	G [dBi]	η [%]	FTBR [dB]
0.5	7	8	8	100	24.8
0.75	7.1	7.9	7.9	100	33.1
1	7.1	7.9	7.9	100	35.8
1.25	7	7.8	7.8	100	33
1.5	7	7.7	7.7	100	29

Table 7 Analysis of the position of the unit-cells for the design surrounded by two rows

Ypos [mm]	BW [%]	D [dB]	G [dBi]	η [%]	FTBR [dB]
0.5	6.7	7.8	7.8	100	17
0.75	6.7	7.7	7.7	100	20.4
1	6.6	7.5	7.5	100	21
1.25	6.6	7.3	7.3	100	21.1
1.5	6.5	7.1	7.1	100	21.5

rows of unit-cells in front of the patches. Table 7 presents the simulated results. The bandwidth, directivity, and gain decreases when the HIS moves away from the patches, while the FTBR improves. The radiation efficiency is maximum for all the Ypos values.

4.4 Optimization and comparison

Finally, from the previous analysis, the designs are compared with each other when the metasurface is placed at its optimal position (see Table 8). Design (W) enhances in directivity, gain and considerably in FTBR compared to the basic array (A), which does not include the metasurface. It is necessary to highlight that these improvements have been achieved without increasing the total size and thickness of the antenna. Introducing the HIS between the patches reduces the coupling between them, which improves the radiation parameters. Considering the surface currents presented in Fig. 6a and b, it can be observed that the value of the surface currents slightly varied, showing higher levels in (W). Moreover, the HIS shows high current levels, especially the central unit-cell. Design surrounded by unit-cells (R) overcomes (W) in bandwidth and notoriously in FTBR whit maximum radiation efficiency. Nevertheless, it exhibits slightly lower directivity and gain values. Figure 6c shows that the surface currents in the patches are different from (W). Furthermore, the central-frontal unit-cells also present high current levels, which translates into bandwidth and FTBR improvements. On the other hand, including a new row of unit-cells, design (2R), does not seem profitable, as the performance remains similar to (A), but the overall antenna size has been increased. In view of the results, the unit-cells size of the

Table 8 Comparison of the designs

Design	BW [%]	D [dB]	G [dBi]	η [%]	FTBR [dB]	A [mm^2]	Fr-HIS [GHz]	Ypos [mm]
(A) Basic array	7	7.4	7.4	98	19	658	–	–
(W) Wall	6.8	8.2	8.2	100	25.4	658	28.4	1
(R) Row	7.1	7.9	7.9	100	35.8	658	28.4	1
(2R) Two Rows	6.6	7.5	7.5	100	21	759	28.4	1
(O) Optimized	7.1	9.2	9.2	100	17	546	27.1	1.125
(O2) Optimized2	7.5	8.5	8.5	100	22.6	658	27.1	1.125
(P1) W-Parasite	7.1	7.8	7.8	100	12.2	658	–	–
(P2) R-Parasite	8.2	6.9	6.9	100	7.1	658	–	–
(P3) 2R-Parasite	9.3	7	7	100	15.5	759	–	–

(2R) design has been varied in order to improve the results. (O) includes unit-cells of Wp=1.6 mm and *g*=0.2 mm. (O) outperforms in bandwidth, directivity and gain the rest of the designs even with a lower size, but the FTBR reduces. In order to determine if the FTBR reduction is related with the size of the ground plane, (O2) recovers the dimensions of (A) with the unit-cells of (O). (O2) retrieves the FTBR and outperforms design (A) in everything, and almost nearly the same occurs to (W), which only overcomes (O2) in FTBR. (O2) surpasses (O) in bandwidth and FTBR. In addition, in order to demonstrate that the metasurface does not act like a parasite, three designs including parasitic arrangements (see Fig. 6e–g), tight to the HIS unit-cells metallization geometry, has been simulated. Results are included in Table 8. The three designs with parasite (P1), (P2), (P3) do not improve

the radiation properties of the antenna, as it can be seen, they show low surface current levels. They only enhance the bandwidth, especially (P3). The FTBR has worsened in all cases. Depending on the requirements, further optimization must be carried out on the combine structure, due to the mutual influence of the array and the HIS, for being arranged on the same layer. Likewise, it is necessary to kept in mind that the resonance frequency of the metasurface arranged with the antenna has varied compared to the infinite structure designed in simulation.

In addition, it is necessary to highlight that the design is technologically advantageous, since the unit-cell does not include vias holes (as many other works using the well-known mushroom-like unit-cell [12]). Moreover, the metasurface has been arranged in the same layer than the
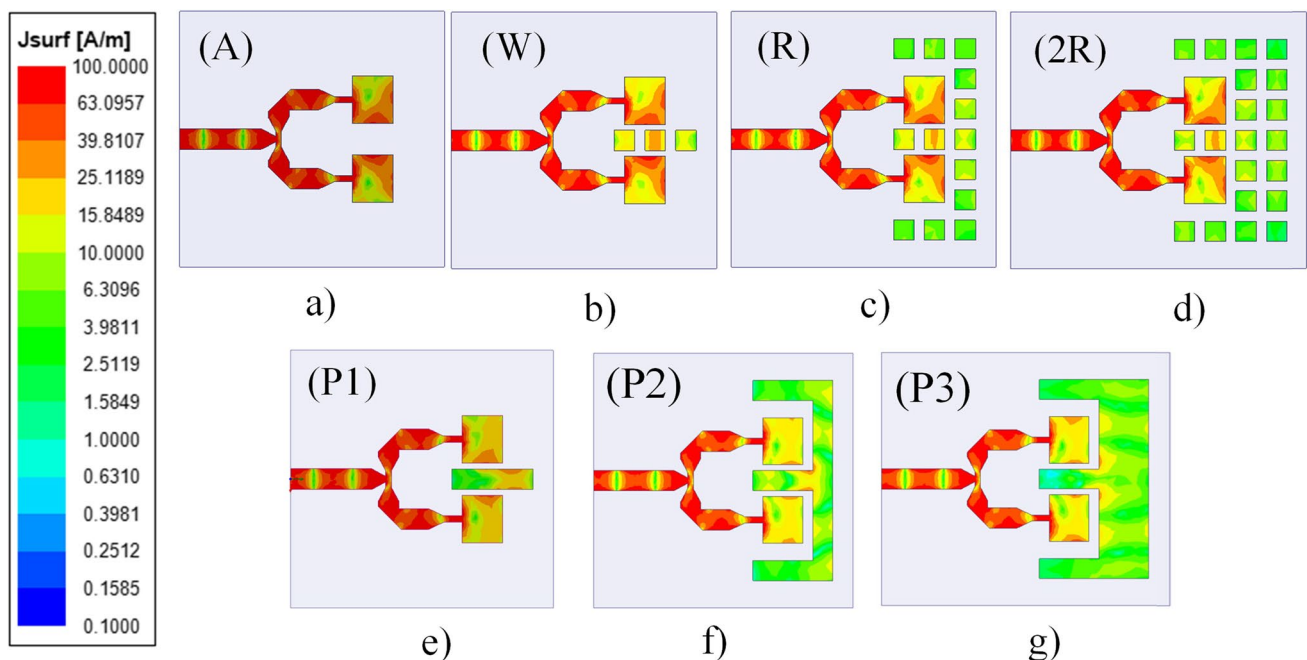
Fig. 6 Surface current distribution for the phase 210∘ **a** Basic Array (A), **b** Wall (W), **c** Row (R), **d** Two Rows (2R), **e** W-Parasite (P1), **f** R-Parasite (P2), **g** 2R-Parasite (P3)

antenna, so that the total thickness of the design has not been increased. Therefore, this work represents an advance in metasurfaces and planar antennas combination and, furthermore, at high frequency.

## 4.5 Fabricated prototypes: comparison between simulation and measurement

Prototypes of both, the basic array (A) and the optimized design with metasurface (O), have been manufactured using laser micromachining (see Fig. 7a and b). Although the prototypes exhibit proper impedance matching in the intended frequency band, the resonance frequency has slightly shifted with respect to simulations, as it can be observed in Fig. 7c. The discrepancies between simulation and measurement results are attributable to several issues. It is necessary to highlight that the connector is soldered by hand to a narrow strip, which can produces these mismatches, as it is not possible to ensure that the edge of the connector is at the same distance from the edge of the board in all prototypes. Furthermore, it is notable that the connector is very large compared to 24.15 GHz patch size, and therefore, it can influence the measurement. Slightly variation in the size of the patches and in the dimensions of the metallization of the unit-cell or in the gap of the metasurface, can produce these mismatches. The manufacturing tolerances in Lp shift the resonance frequency. An increase of 0.15 mm compared to the original Lp size (over-etching in fabrication) shifts the

resonance frequency 200 MHz downwards which, together with the other effects, could explain the shift of the Basic Array curve. A smaller metallization size of the unit cells (under-etching in fabrication) or a wider gap shift the resonance frequency of the metasurface upwards and therefore, the Array-HIS one. Nevertheless, the measured trace for the Basic Array has shifted by 1.7% compared to the simulated one, while the measured one for the Array-HIS has shifted by 0.4% compared to the one obtained in simulation. Furthermore, both antennas are operative in the 24.05–24.25 GHz license free frequency band.

Measurements have been performed in a wide frequency range (1–40 GHz) anechoic chamber despite the challenge of measuring such small antennas in a chamber not intended for mmWave testing, due to potential reflections caused by absorbers size, positioners, etc. as it can be observed in Fig. 7d. Figure 8a and b respectively show the radiation pattern cuts for E (Phi=90∘) and H (Phi=0°) planes for the basic array and the array-HIS. In both cases, fairly good agreement is observed regarding simulation and measurement results for the H-plane. Nevertheless, for the E-plane there are discrepancies for both antennas, due to the higher cross-polarization and the deformation of the copolar component in the measurement results compared to the simulation ones. These discrepancies are due to several reasons. On the one hand, the corporate-fed induces high cross-polarization at higher frequencies. On the other hand, the 3D printed polylactic acid (PLA) gadget, used to place the
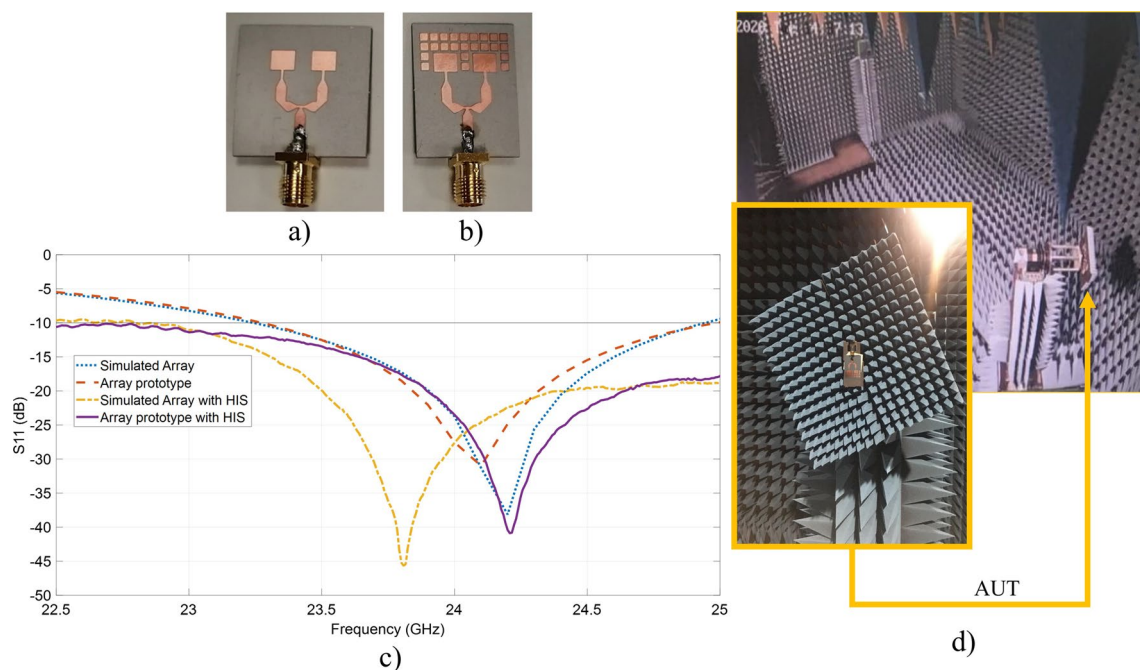
Fig. 7 **a** Basic array prototype. **b** Array-HIS prototype. **c** Simulated and measured reflection coefficient for the Basic Array and the Array-HIS. **d** Measurement set-up in the anechoic chamber
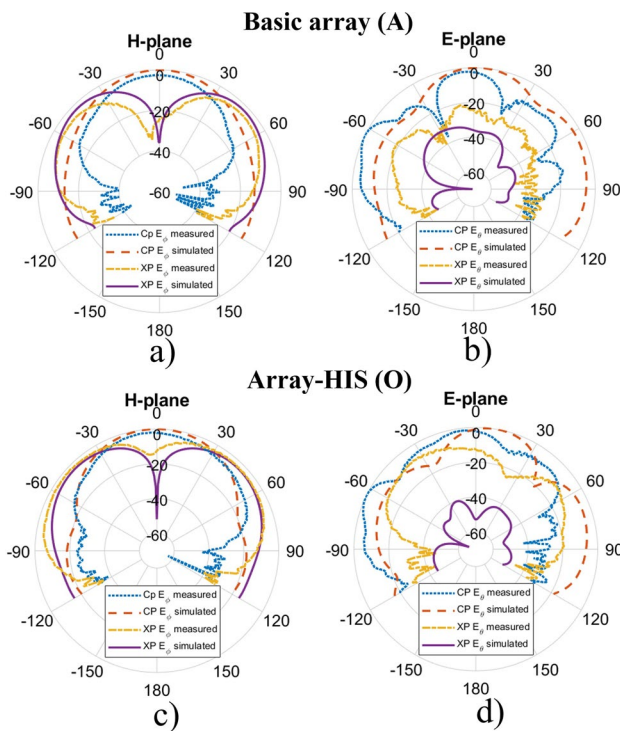
Fig. 8 Radiation pattern cuts measured for the Array-HIS. **a** Basic Array radiation pattern cuts. **b** Array-HIS radiation patter cuts

Table 9 Basic array and array-HIS simulated and measured radiation properties

Desing	Simulation			Measurement
	D [dB]	G [dBi]	η [%]	G [dBi]
Basic Array	7.4	7.3	98	7.4
Array-HIS	9.2	9.2	100	9

prototype during the measurement can produce reflections, which negatively influence the measurement.

Gain transfer method has been used to estimate the peak realized gain of the antennas (see Table 9). This method consists of the intercomparison of the antenna under test (AUT, basic array or array-HIS) with a sounding antenna of known characteristics (in this case it was used the Standard gain horn 20240-25 manufactured by Flann Microwave). Discrepancies between simulated and measurement results can be due to many factors. On the one side, as it was already mentioned, the prototype connector effect, the measurement cable, or the plastic attachment. On the other side, those sources of uncertainty in gain measurement like misalignment between AUT-probe, multipath, reflections or impedance mismatch of antennas [31].

4.6 Comparison with the State of the Art

In order to validate and endorse the achievements of this work, a comparison of the optimized array-HIS antenna with the state-of-the-art antennas at 24 GHz is performed. Table 10 contains the main information, radiation properties and bandwidth, for a fair evaluation. It is necessary to remark that most of the references do not provide the radiation efficiency, although this is a key parameter for wearable, from both an operational and an economically perspective, concerning the batteries. The optimized array-HIS (O), overcomes [32] in size, as well as in bandwidth and gain, even using [32] thicker substrate and lower relative dielectric permittivity. [33] presents a complex four-layer design, which is outperform by (O) in bandwidth and gain, with maximum radiation efficiency. Compared to [34], (O) presents a more compact design with wider bandwidth, however [34] shows slightly higher gain. Concerning [35]

Table 10 Comparison of the proposed array-HIS antenna with the state-of-the-art antennas at 24 GHz

Ref	Dim [mm]	ϵ_r	Freq [GHz]	Bandwidth [%]	Gain [dBi]	η [%]
[32]	$30 \times 30 \times 2.6$	1.2	24	1.2	5.1	–
[33]	$6.8 \times 6.8 \times 0.26$	3	24	2	5.44	–
[34]	$90 \times 25 \times 0.203$	3.55	24	1.6	11	–
[35]	$20 \times 25 \times 0.23$	2.9	24	2.3	7.4	35
[36]	$24 \times 24 \times 1.6$	6.4	24	8	9	–
[37]	$23.2 \times 68 \times 0.203$	3.55	28	12.5	12	85
[38]	$10 \times 4 \times 0.3$	1.95	24	16.7	4.6	73
[39]	$10 \times 10 \times 0.787$	2.2	24.8	1.32	6.48	–
[39]	–	2.2	23.2	1.18	12.3	–
[40]	$20 \times 17 \times 1.575$	2.2	28	2.57	8.39	84.5
This work (O)	$26.7 \times 20.4 \times 0.8$	3	24	7.1	9.2	100

with similar relative dielectric permittivity, (O) shows higher gain and much higher radiation efficiency. (O) outperforms [36] since using a substrate with half the thickness and relative dielectric permittivity, provides almost the same bandwidth and gain. Thus, similar performance is achieved with (O), being thinner and cost reduced. Regarding [37], this design provides higher bandwidth, however the resonance frequency is higher than for (O). Moreover, it shows slightly higher gain, despite being a 1×4 element array and the radiation efficiency is much lower. (O) overcomes [38] notoriously in gain and in radiation efficiency. In comparison with [39], (O) outperforms in bandwidth both designs, the patch element and the array, even using higher relative dielectric permittivity, it shows higher gain than the element. Moreover, (O) exhibits slightly less gain that the 1×4 element array. Finally, (O) overpasses [40] in bandwidth even using the later a thicker substrate. In addition, (O) provides higher gain and radiation efficiency than [40].

5 Conclusions

A compact and lightweight operative array-HIS antenna in the 24 GHz frequency band has been achieved. Different arrangements and number of HIS unit-cells with the patch array have been analyzed. The results obtained have been satisfactory, as the combination of the metasurface with the array improves the radiation parameters of the antenna and the bandwidth. From the analysis it is concluded that once both, the patch array and HIS, are operating at the desired frequency, the optimization must be performed on the combined structure, due to the mutual influence between them, for being arranged at the same layer. In addition, there is an optimal distance of the unit-cells from the front edge of the patches, at which optimum performance is obtained. It was also observed that as the periodicity of the metasurface increases, it is necessary to vary the unit-cell dimensions to optimize the radiation parameters of the antenna, since the resonance frequency of the metasurface shifts. It has been shown that adding a parasite does not provide the benefits of introducing a metasurface. It only enhances the bandwidth, but it worsens the radiation parameters of the antenna. The metasurface improves the characteristics of the antenna or at least preserves them. It is necessary to highlight that all the designs show high radiation efficiency, which is key for wearable in order to save battery. Moreover, the final array-HIS antenna results economically and technologically advantageous, since including the metasurface in the same layer than the antenna does not increase the cost of the manufacturing neither the complexity of it.

Declarations

References

1. I.M. Skolnik, *Introduction to RADAR Systems* (McGraw-Hill, New York, 1980)
2. T.S. Rappaport et al., IEEE Access **1**, 335 (2013). https://doi.org/10.1109/ACCESS.2013.2260813
3. B.K.J. Al-Shammari, I. Hburi, H.R. Idan, H.F. Khazaal, 2021 ICICT (Basrah, Iraq), **133**, (2021). https://doi.org/10.1109/ICICT52195.2021.9568459
4. V.K. Kukkala, J. Tunnell, S. Pasricha, T. Bradley, IEEE CTSoc Mag. **7**, 18 (2018). https://doi.org/10.1109/MCE.2018.2828440
5. S. Jardak, M. Alouini, T. Kiuru, M. Metso, S. Ahmed, IEEE AESS Mag. **34**, 36 (2019). https://doi.org/10.1109/MAES.2019.180130
6. M. Marcus, B. Pattan, IEEE Microw. Mag. **6**, 54 (2005). https://doi.org/10.1109/MMW.2005.1491267
7. M. Ferreira, P. Pinho, 2021 ConfTELE (Leiria, Portugal), **1**, (2021). https://doi.org/10.1109/ConfTELE50222.2021.9435524
8. S. Claflin, M.A. Ul Alam, 2020 IEEE URTC (Massachusetts, USA), **1**, (2020). https://doi.org/10.1109/URTC51696.2020.9668894
9. S. Kharkovsky, J.T. Case, M.A. Abou-Khousa, R. Zoughi, F.L. Hepburn, IEEE Trans. Instrum. Meas. **55**, 1250 (2006). https://doi.org/10.1109/TIM.2006.876543
10. S.S. Ahmed, IEEE J. Microw. **1**, 191 (2021). https://doi.org/10.1109/JMW.2020.3035790
11. X. Yi et al., IEEE Access **7**, 48053 (2019). https://doi.org/10.1109/ACCESS.2019.2904493
12. D. Sievenpiper, L. Zhang, R.F.J. Broas, N.G. Alexopolous, E. Yablonovitch, IEEE Trans. Microw. Theory Tech. **47**, 2059 (1999). https://doi.org/10.1109/22.798001
13. Deepti, D. Gangwar, S. Singh, A. Sharma, S.P. Singh, A. Lay-Ekuakille, Sens. Actuator A Phys 333, (2022). https://doi.org/10.1016/j.sna.2021.113273

14. H.F. Álvarez, M.E. de Cos, S. García, F. Las-Heras, Sens. Actuator A Phys. **272**, 223 (2018). https://doi.org/10.1016/j.sna.2018.01.026

15. T.M. Hossain, M.F. Jamlos, M.A. Jamlos, F. Dzaharudin, M.Y. Ismail, S.S. Al-Bawri, S. Sugumaran, M.N.A. Salimi, Sens. Actuator A Phys. (2020). https://doi.org/10.1016/j.sna.2019.111638

16. H.F. Alvarez, M.E. de Cos Gomez, J.J. Garcia, F. Las-Heras, 2020 AP-S/URSI (Montréal, Québec, Canada), 859 (2020). https://doi.org/10.1109/IEEECONF35879.2020.9330343

17. S.N. Burokur, A.C. Lepage, S. Varault, X. Begaud, G.P. Piau, A. de Lustrac, Appl. Phys. A **122**, 326 (2016). https://doi.org/10.1007/s00339-016-9885-1

18. M. Mantash, A. Kesavan, A. Denidni, IEEE Antennas Wirel. Propag. Lett. **17**, 29 (2018). https://doi.org/10.1109/LAWP.2017.2772222

19. R. Karimian, A. Kesavan, M. Nedil, T.A. Denidni, IEEE Antennas Wirel. Propag. Lett. **16**, 373 (2017). https://doi.org/10.1109/LAWP.2016.2578179

20. A. De Sabata, L. Matekovits, A. Silaghi, Printed Periodic Structures in Support to 5G Network Antennas, Printed Antennas for 5G Networks, **77** (2022). https://doi.org/10.1007/978-3-030-87605-0_4

21. A. Kumar, A.Q. Ansari, B.K. Kanaujia, J. Kishor, L. Matekovits, Radio Sci. (2021). https://doi.org/10.1029/2020RS007222

22. O. Sokunbi, H. Attia, Prog. Electromagn. Res. C **100**, 233 (2020). https://doi.org/10.2528/PIERC19112607

23. M. Bilal, S.I. Naqvi, N. Hussain, Y. Amin, N. Kim, Electronics (2022). https://doi.org/10.3390/electronics11060962

24. Y. Alnaiemy, T.A. Elwi, L. Nagy, Period. Polytech. Elec. Eng. Comp. Sci. **63**, 332 (2019). https://doi.org/10.3311/PPee.14379

25. I.A, d.R. C, IEEE AP-S 1B, **582**, (2005). https://doi.org/10.1109/APS.2005.1551291

26. C.A. Balanis, *Antenna Theory: Analysis and Design*, 3rd edn. (John Wiley & Sons, 2005)

27. R. Garg, P. Bhartia, I. Bahl, A. Ittipiboon, *Microstrip Antenna Design Handbook* (Artech House, Boston, 2001)

28. D.M. Pozar, *Microwave Engineering* (Wiley, Hoboken, 2012)

29. F. Capolino, *Theory and Phenomena of Metamaterials* (CRC Press, 2009)

30. M.E. de Cos, F. Las-Heras, Appl. Phys. A **118**, 699 (2015). https://doi.org/10.1007/s00339-014-8782-8

31. "IEEE Standard Test Procedures for Antennas," ANSI/IEEE Std 149-1979, pp. 1-144, (30 Nov. 1979). https://doi.org/10.1109/IEEESTD.1979.120310

32. M. Cupal, Z. Raida, 2017 ICEAA (Verona, Italy), **1154**, (2017). https://doi.org/10.1109/ICEAA.2017.8065472

33. H. Dawood, M. Zahid, H. Awais, S. Shoaib, A. Hussain, A. Jamil, 2020 ICECCE (Istanbul, Turkey), 1 (2020). https://doi.org/10.1109/ICECCE49384.2020.9179186

34. C.-H. Kuo, C.-C. Lin, J.-S. Sun, IEEE Antennas Wirel. Propag. Lett. **16**, 1731 (2017). https://doi.org/10.1109/LAWP.2017.2670231

35. P. Mezzanotte, C. Mariotti, M. Virili, M. Poggiani, G. Orecchini, F. Alimenti, L. Roselli, I.E.T. Sci, Meas. Tech. **8**, 342 (2014). https://doi.org/10.1049/iet-smt.2013.0279

36. F.A. Ghaffar, M.U. Khalid, K.N. Salama, A. Shamim, IEEE Antennas Wirel. Propag. Lett. **10**, 705 (2011). https://doi.org/10.1109/LAWP.2011.2161600

37. Y. Liu, M.C.E. Yagoub, M. Nassor, 2020 AP-S Symposium (Montréal, Québec, Canada), **33**, (2020). https://doi.org/10.23919/USNC/URSI49741.2020.9321630

38. M. Wagih, A.S. Weddell, S. Beeby, 2021 URSI GASS (Rome, Italy), **1**, (2021). https://doi.org/10.23919/URSIGASS51995.2021.9560643

39. K. Bangash, M.M. Ali, H. Maab, H. Ahmed, 2019 ICECCE (Swat, Pakistan), **1**, (2019). https://doi.org/10.1109/ICECCE47252.2019.8940807

40. L.C. Paul, M.H. Ali, N. Sarker, M.Z. Mahmud, R. Azim, M.T. Islam, 2021 ICIEV and icIVPR (Kitakyushu, Japan), **1**, (2021). https://doi.org/10.1109/ICIEVicIVPR52578.2021.9564160